Polarized Raman study of the phonon dynamics in $Pb(Mg_{1/3}Nb_{2/3})O_3$ crystal

Oleksiy Svitelskiy* and Jean Toulouse
Department of Physics, Lehigh University, Bethlehem, Pennsylvania 18015, USA

Grace Yong
Lafayette College, Easton, Pennsylvania 18042, USA

Z.-G. Ye
Department of Chemistry, Simon Fraser University, Burnaby, British Columbia, Canada V5A 1S6
(Received 20 January 2003; revised manuscript received 27 May 2003; published 17 September 2003)

$Pb(Mg_{1/3}Nb_{2/3})O_3$ is one of the simplest members of the class of lead relaxors and often serves as a model system for more complicated compounds. In this paper, we analyze both polarized and depolarized Raman-scattering spectra, measured in the temperature range between 1000 and 100 K, using a multiple-peak decomposition. Based on this analysis, we propose a comprehensive picture of the structural transformations in the crystal and associated dynamics. According to our model, the formation of the $Fm\bar{3}m$ symmetry in the chemically ordered regions as well as the appearance and freezing of the polar nanoregions are the consequences of the same phenomenon: the off-centered displacements of ions and their fast reorientational thermal motion. Short-lived dynamic lattice distortions are present even at the highest measured temperatures. From the Burns temperature, $T_d \sim 620$ K, their motion becomes progressively more restricted. Temperature $T^* \sim 350$ K marks the beginning of the freezing process which continues down to the temperature of the electric-field-induced phase transition, $T_{d0} \sim 210$ K. Raman scattering exists due to the presence of local lattice distortions. It is characterized by phonons with different wave vectors interacting with dynamic and static disorder.

DOI: 10.1103/PhysRevB.68.104107 PACS number(s): 77.80.−e, 78.30.−j, 63.20.Kr, 77.22.Gm

I. INTRODUCTION

$Pb(Mg_{1/3}Nb_{2/3})O_3$ (PMN) is one of the earliest members of the growing family of lead ferroelectric relaxors, which, due to its application potential, has been attracting attention of researchers for many years. However, despite significant efforts, many properties of lead compounds are still unclear and the very nature of the relaxor behavior has yet to be understood. The difficulties stem from the complexity of these materials with a high degree of compositional, chemical, and structural disorder (for review, see Ref. 1).

$Pb(Mg_{1/3}Nb_{2/3})O_3$ has a perovskite structure with (on average) a cubic $Pm\bar{3}m$ symmetry, with Mg^{2+} and Nb^{5+} ions interchanging on *B* sites. Measurements of the dielectric constant show that the crystal does not undergo a sharp transition to a ferroelectric phase. Instead, the dielectric constant exhibits a broad maximum at $T_{\max} \sim 270$ K.[2] Below $T_d \sim 620$ K, it deviates from Curie-Weiss law[3] and, at $T \lesssim 350$ K, exhibits strong frequency dispersion.[4] The structure of PMN is not homogeneous. If Mg and Nb occupation ratio was uniformly and ideally equal (1:2) throughout the crystal, it would have a rhombohedral symmetry ($R3m$). But, a network of superstructure clusters with face-centered cubic symmetry ($Fm\bar{3}m$) destroys the picture. The size of these clusters is of the order of 2–3 nm; the distance between the centers of neighboring clusters is ~ 2.5 nm.[5,6]

The most widely accepted hypothesis, so-called "space-charge model," associates the $Fm\bar{3}m$ clusters with antiferroelectrically ordered[7] regions where the Mg:Nb occupation ratio is equal to 1:1, i.e., with local composition $Pb(Mg_{1/2}Nb_{1/2})O_3$.[8,9] Such 1:1 clusters carry an excessive negative charge, which is compensated by the positively charged host matrix. The network of such charges acts as a source of random fields and may prevent the occurrence of a "normal" phase transition. Alternatively, the $Fm\bar{3}m$ clusters might be explained by a local order in the form of $Pb[B^{2+}_{1/2}B^{5+}_{1/3}]_{1/2}[B^{5+}]_{1/2}O_3$.[10,11] This hypothesis avoids assumption of considerable space charges and calls for other reasons to explain the relaxor behavior, including random fields due to disorder-induced local anisotropy,[12] effects related to different ionic radii,[13] or both.[14] To establish the correct model, additional investigations are needed.

The presence of areas with a special order causes the crystalline structure to change in an intricate way. In the high-temperature limit, the crystal has a uniform primitive cubic ($Pm\bar{3}m$) structure. Lowering the temperature leads to the distinguishability between Mg^{2+} and Nb^{5+} sites and to the formation in the chemically ordered regions of a face-centered ($Fm\bar{3}m$) superstructure. The temperature, when these $Fm\bar{3}m$ clusters form, is yet to be determined. Husson's data suggest their presence at $T \sim 850$ K.[15] Our data (see below) raise the upper limit to a temperature higher than 1000 K.

Cooling the sample leads to the nucleation of polar nanoregions (PNR's) characterized by local distortions. These distortions are responsible for the deviation of the dielectric constant from a Curie-Weiss law at T_d.[3] Their presence also causes a nonlinearity in the temperature dependence of the optical refractive index.[16] The size of the PNR's is ~ 30–80 Å, depending on temperature.[17] The appearance of

TABLE I. Interpretations of Raman-scattering spectrum from PMN offered by various research groups. Note, many of the entries in the table mutually exclude each other.

Research Group	45 cm^{-1}	130 cm^{-1}	260 cm^{-1}	420 cm^{-1}	500–600 cm^{-1}	780 cm^{-1}
Husson (Ref. 15) (1990)	Pb-O Stretching modes		O-B-O Bending	Mg-O-Mg Stretching	Nb-O . . . Nb Stretching	Nb-O . . . Mg Stretching
Dimza (Ref. 42) (1992)						Coexistence of tetragonal and rhombohedral phases
Krainik (Ref. 27) (1993)	TO_1					
Idink (Ref. 41) (1994)	All spectrum is due to one phonon processes, originates from rhombohedral symmetry clusters and consists of nine modes					
Marssi (Refs. 28–31) (1996-98)	TO_1	TO_2	TO_3	TO_4		TO_2+TO_4 or LO_4 (1996) Nb-O-Mg or LO_4 (1998)
Jiang (Ref. 33) (1999)	Due to positional disorder of lead			Due to $Fm\bar{3}m$ clusters and vibration of oxygen octahedra		
Lushnikov (Refs. 34,35) Siny (Refs. 36–40) (1999)	All spectrum originates from $Fm\bar{3}m$ clusters, similarly to the case of $PbSc_{1/2}Ta_{1/2}O_3$ VV-E_g?? VH-$2T_2g$ or VV and one VH have fractal character another VH-T_{2g}		Disorder-induced scattering from silent modes and second-order scattering			A_{1g} Breathing mode of oxygen
Dujovne (Ref. 32) (2002)	TA+disorder					

polar distortions is a consequence of the ion off-centering that is a common property of many perovskites. By structural similarity, one could expect that the mechanism of the polar region's formation in PMN is analogous to the one in $KTa_{1-x}Nb_xO_3$ (KTN).[18] However, unlike KTN where Nb^{5+} is the only off-centered positive ion, PMN represents a more difficult case. Here, not only *both ions of B type*, Mg^{2+} and Nb^{5+}, are shifted by $\sim 0.1–0.2$ Å, but also Pb^{2+}, *the ion of A type*, is off-centered by $\sim 0.25–0.35$ Å.[19–23] The *B* ions tend to shift along a (111) direction, thus having eight equivalent positions. The shifts of the Pb^{2+} ions exhibit a spherically symmetric distribution.[23] It is often assumed[12–15] that Nb^{5+}, due to its position in the cell and small radius, acts as the main ferroelectric agent.

At high temperatures, the off-centered ions are free to reorient among all allowed off-centered positions. Cooling down and the growing role of the dipole interactions cause the appearance of correlated regions, consisting of several neighboring cells. Each such region is characterized by a giant electric dipole moment and a local distortion from the cubic symmetry. The PNR's are capable of reorientational motion as whole units. In KTN, for sufficiently high Nb concentrations, the development of these regions leads, at some critical temperature, to a phase transition. However, in PMN, the polar regions develop under constraints imposed by the local anisotropy. As a result, no ferroelectric phase transition, but a glasslike freezing of the polar regions, is observed.[12] A bias electric field of magnitude ~ 1.8 kV/cm, applied in the (111) direction, is sufficient to compensate for the frustrating effects and to induce, at $T_{d0} \sim 210$ K, a transition to the rhombohedral $R3m$ ferroelectric phase.[24]

Raman spectra of PMN have been measured and reported by several research groups.[15,25] But, the site disorder, the presence of chemically ordered regions, the off-center ionic displacements, and the resulting high complexity of the scattering processes have caused difficulties in their interpretation. Although in cubic crystals first-order Raman scattering is prohibited by symmetry, the above-mentioned factors result in the major spectral lines observed having a first-order character but broadened by the disorder.[26] In particular, the question of the soft ferroelectric mode (TO_1) and the strong Raman line at ~ 45 cm^{-1}, which is close to where TO_1 is expected to be found, has been a stumbling block for investigators. The interpretations of the PMN Raman spectrum offered by various research groups are summarized in Table I. As seen in the table, these interpretations are often mutually exclusive, ranging from those that explain the light scattering by *disorder in general* (groups of Husson,[15] Krainik,[27] Marssi,[28–31] and Dujovne[32]) to those that connect it to the presence of some *particular type of disorder*, which can lead to the appearance of clusters with face-centered cubic (groups of Jiang,[33] Lushnikov,[34,35] and Siny[36–40]), rhombohedral (Idink[41]), or tetragonal (Dimza[42]) symmetry. The assignment of particular lines is even more contradictory. A detailed review on this subject is presented in Ref. 40. The close similarity between the Raman spectra of the PMN and of the ordered $PbSc_{1/2}Nb_{1/2}O_3$ and $PbSc_{1/2}Ta_{1/2}O_3$ crystals (compare, e.g., with Ref. 43) points out the importance of the 1:1 ordered regions for the light-scattering processes.

Recently published low branches of phonon-dispersion curves,[44–47] measured by neutron scattering, can be helpful for the phonon assignment of some of the Raman lines. Ac-

cording to these data, the strong 45–cm^{-1} line has an energy close to the energy of the zone-center (ZC) TO_1 or the zone boundary (ZB) TA phonon, propagating in $\langle 100 \rangle$ direction. Therefore, the presence of a strong light scattering in the depolarized geometry points out the importance of the disorder-related processes. Lowering the temperature, the TO_1 zone-center phonon exhibits softening, at $T \sim T_d$, and a drastic increase in damping leads to its disappearance. This overdamping persists down to $T_{d0} \sim 210\ K$.[44] It also causes a significant, almost sixfold, broadening of the TA phonon branch.[48] It would therefore seem reasonable to expect that the Raman line at 45 cm^{-1} should also be affected. However, none of the known Raman reports show any sign of such an overdamping of this line. Neither is it observed in the infrared spectra.[49]

The formation of the $Fm\bar{3}m$ clusters and/or PNR's is accompanied by the appearance of relaxational and reorientational dynamics. This dynamics can be reflected in the light-scattering spectrum either directly or, indirectly, through interaction with the phonon modes. This was demonstrated in earlier works on the central peak (CP) in PMN (Ref. 50) and related materials [e.g. model relaxor $KTa_{1-x}Nb_xO_3$ (Refs. 51–57)]. A careful Fabry-Perot study of several $KTa_{1-x}Nb_xO_3$ crystals[51,54] has to be mentioned separately, since it allowed to model the CP as a result of relaxations coupled to the soft mode.[57] Theoretical considerations[58] show that the appearance of the central peak in the Raman spectrum is not the only consequence of this internal relaxational motion. Interactions of this motion with phonons can cause their damping and softening.[58] These predictions have been tested on several types of crystals with internal degrees of freedom, such as alkali-halide-cyanide $[K(CN)_x\text{-}KBr_{1-x}, K(CN)_x\text{-}KCl_{1-x}]$ (Refs. 59–62) compounds. Recently, we have analyzed[63] the reorientational motion in ferroelectric $KTa_{1-x}Nb_xO_3$ crystals.

In the present, paper we continue this work and discuss the role of the relaxational and reorientational dynamics in the scattering processes from a PMN crystal. We offer a complex analysis of the temperature dependencies of the polarized (VV) and depolarized (VH) Raman spectra from a single crystalline PMN sample. This analysis is based on the multiple-peak decomposition suggested by Siny *et al.*[50] However, to obtain a more complete picture, we have extended our study to a higher spectral (up to 1000 cm^{-1}) and broader temperature range (from 100 to 1000 K) . We interpret our results in light of recently published neutron-scattering data and use the concept of the interaction of phonons with internal relaxational motion. As a result of this work, we present a comprehensive picture of the structural transformations in PMN and the origin of its Raman spectrum.

II. EXPERIMENTAL SETUP AND RESULTS

We have investigated Raman scattering from a $\langle 100 \rangle$-cut PMN single crystal. The crystal was grown by the high-temperature solution technique using 30 wt % PbO as flux. The growth conditions were optimized based on the pseudo-binary phase diagram established for PMN and PbO.[64] The

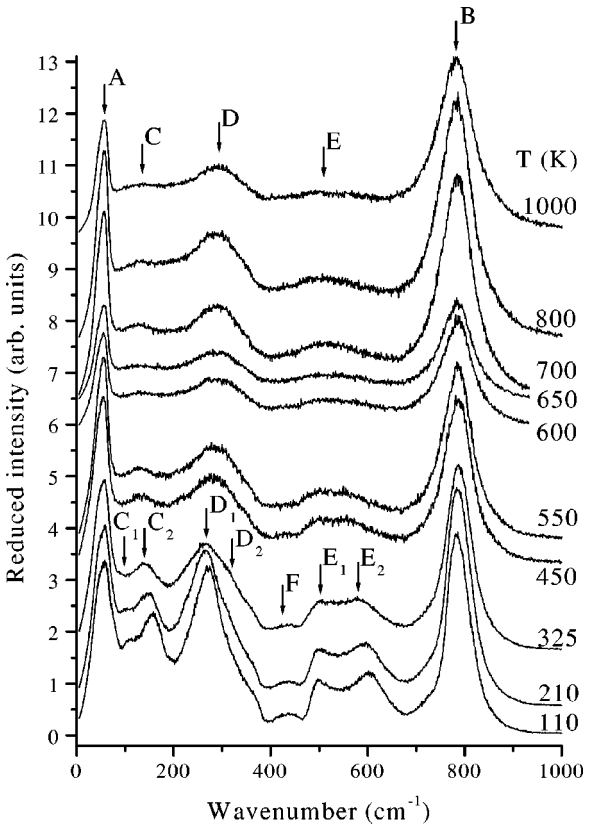

FIG. 1. Examples of Raman-scattering spectra measured at various temperatures without polarization analysis and corrected by the population factor.

as-grown crystal exhibits a pseudocubic morphology with $\langle 100 \rangle$ cubic growth steps. A $\langle 100 \rangle / \langle 110 \rangle$ cubic-oriented crystal of a volume of 53 mm^3 was cut from a large as-grown crystal and polished with fine diamond paste (down to 0.25 mm). It showed very high optical quality and satisfied the requirements for light-scattering studies. The scattering was excited by propagating, in a $\langle 100 \rangle$ direction, 514.5-nm light from a 200-mW Ar^+-ion laser focused to a 0.1-mm spot. The scattered light was collected at an angle of 90° with respect to the incident beam (i.e., in $\langle 010 \rangle$ direction) by a double-grating ISA Jobin Yvon spectrometer equipped with a Hamamatsu photomultiplier *R*-649. For most of the measurements, the slits were opened to 1.7 cm^{-1}. However, in order to acquire more precise data in the central peak region, at temperatures close to the maximum of the dielectric constant ($100 < T < 350$ K), the slits were narrowed to 0.5 cm^{-1}. Each polarization of the scattered light, $\langle x|zz|y \rangle$ (VV) and $\langle x|zx|y \rangle$ (VH), was measured separately. In order to exclude differences in sensitivity of the monochromator to different polarizations of light, a circular polarizer was used in front of the entrance slit. For control purposes, we also took measurements without polarization analysis. To protect the photomultiplier from the strong Rayleigh scattering, the spectral region from -4 to $+4$ cm^{-1} was excluded from the scans. The data were collected in the temperature range from 1000 to 100 K. The cooling rate was 0.5–1 K/min. Every 50–20 K the temperature was stabilized and the spectrum recorded. In agreement with a previous paper,[25] we noted

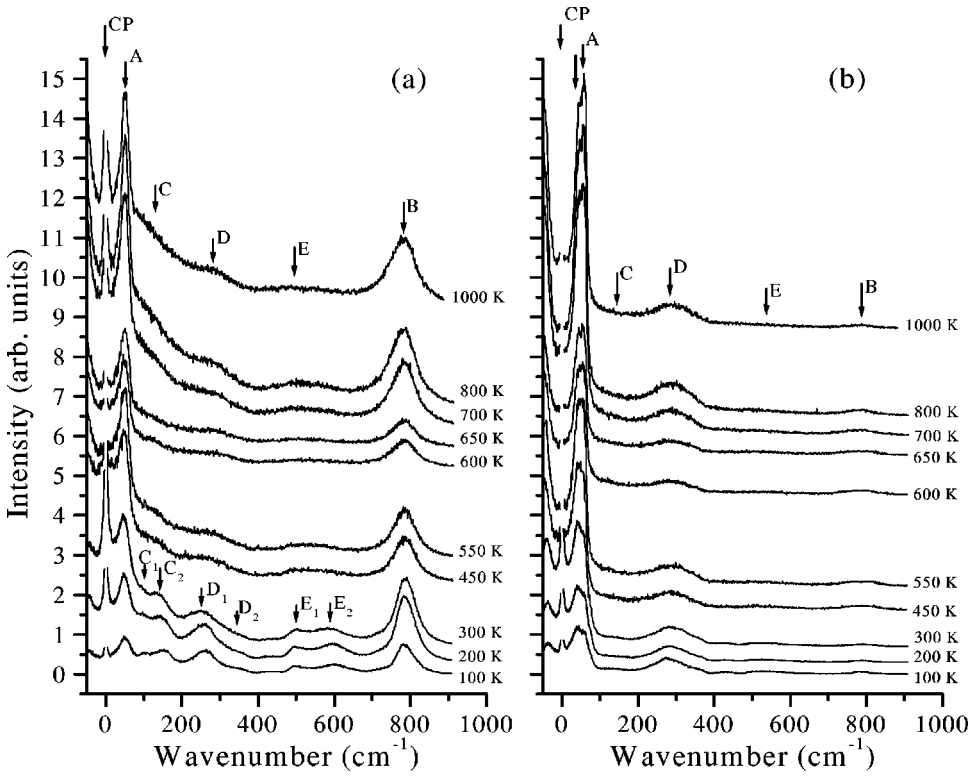

FIG. 2. Examples of Raman-scattering spectra measured in VV or $\langle x|zz|y\rangle$ (a) and VH or $\langle x|zx|y\rangle$ (b) geometries upon cooling from 1000 to 100 K.

that, in the temperature range approximately between 200 and 350 K, the spectra exhibited a strong dependence on the cooling rate and other experimental conditions.

Figure 1 presents examples of light-scattering spectra measured at different temperatures without polarization analysis. To facilitate comparison, we corrected the spectra by the Bose population factor:

$$F(f,T)=\begin{cases} n(f)+1, & \text{for Stokes part} \\ n(f), & \text{for anti}-\text{Stokes part,} \end{cases} \tag{1}$$

where

$$n(f)=[\exp(hf/kT)-1]^{-1}.$$

Figure 2 shows scattering spectra measured in VV [panel (a)] and VH [panel (b)] geometries at different temperatures. These spectra we present in their uncorrected, ''as-measured'' form.

Our spectra (Figs. 1 and 2) are consistent with those from Refs. 15 and 25. In the high-temperature region, a typical spectrum consists of two strong lines centered approximately at 45 cm^{-1} and 780 cm^{-1} (labeled *A* and *B*) and of three broad bands (*C*, *D*, *E*). Line *A* exhibits a fine structure (see Figs. 2 and 3). Lowering the temperature leads to the splitting of the broad bands *C*, *D*, and *E* into pairs of narrower lines (labeled 1 and 2) and to the appearance of a new line *F*.

As seen in Fig. 1, starting from 1000 K, the reduced scattering intensity first grows until the temperature of $\sim$700 K, then sharply decreases to reach a minimum close to the Burns temperature $T_d \approx 620$ K, after which it increases again. At $\sim$550 K, it has grown back to its original strength. Below this temperature, the intensities of the major lines (especially *A* and *B*) are determined primarily by the Bose factor, i.e., after correction they do not show significant temperature changes, demonstrating a characteristic first-order behavior. The similarity in the shape of the low- and high-temperature spectra shows that, even at 1000 K, the scattering exhibits a first-order character. In the perfectly cubic crystal, first-order scattering is prohibited. Therefore, one should assume the presence of distortions in the form of lower symmetry clusters. At high temperature, the clusters must be dynamic, having short lifetimes. Lowering the temperature, their lifetime increases, and below T_d they become longer lived. The observed decrease in Raman intensity around T_d is also seen in Fig. 2. This intensity drop marks a worsening of the optical quality of the crystal, which is consistent with the appearance of $Fm\bar{3}m$ and polar clusters. From a comparison with a related system, KTN (see below), there are reasons to believe that the PNR's have a time-averaged internal tetragonal symmetry. This coexistence of symmetries is quite compatible, since randomly oriented tetragonal PNR's can result in a macroscopic (spatially averaged) $Fm\bar{3}m$ symmetry. Below $T^* \sim 350$ K (which is also close to where the dispersion of the dielectric constant appears), the broad *C*, *D*, and *E* peaks show splitting. This splitting grows with further decrease of the temperature down to $T_{d0} \sim 210$ K, which is the temperature at which a transition can be induced by an external electric field.[24] Finally, below T_{d0}, the shape of the spectra is relatively stable.

A comprehensive analysis of our data and their comparison with the results of other experiments allows us to understand the meaning of the above-mentioned temperatures $T_d \approx 620$ K, $T^* \approx 350$ K, and $T_{d0} \approx 210$ K in the temperature evolution of the Raman spectra and the lattice structure.

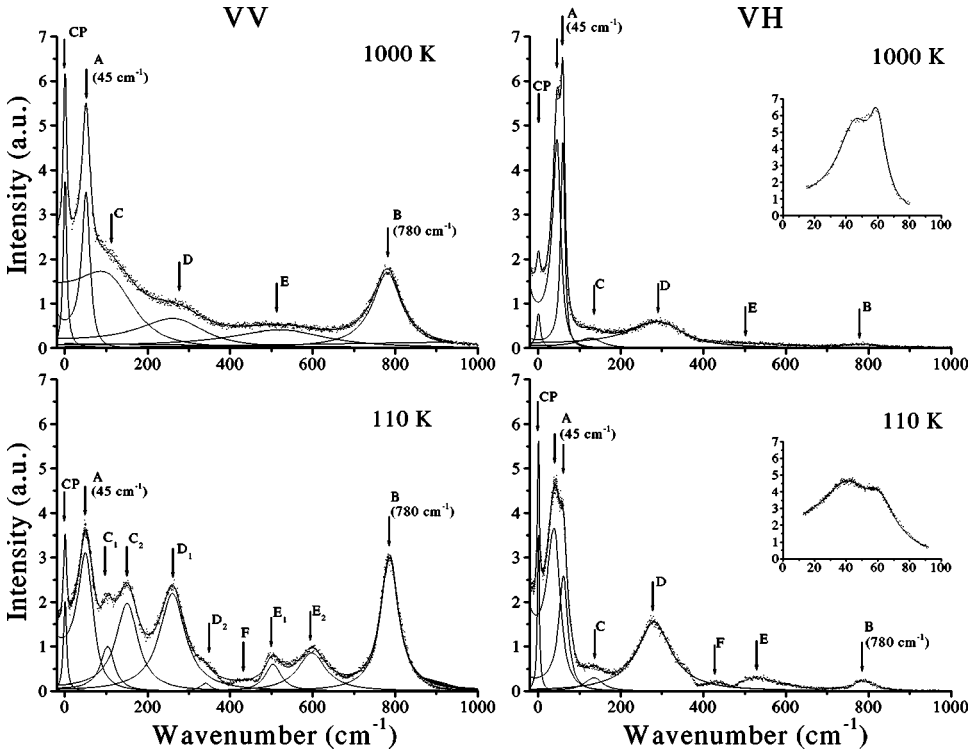

FIG. 3. Examples of multiple-peak decomposition of Raman spectra measured at 1000 and 110 K both in VV (or $\langle x|zz|y\rangle$) and VH (or $\langle x|zx|y\rangle$) geometry. For convenience, major peaks are labeled with letters. Insets show examples of fits for the line *A* using the model of the two coupled harmonic oscillators, as described in discussion.

III. MULTIPLE-PEAK DECOMPOSITION OF SPECTRA PROCEDURE

In order to analyze the data, we decomposed the measured spectra using a multiple-peak fitting procedure. Satisfactory fits could be achieved with the assumption of a Lorentzian central peak and other peaks described by the spectral response functions of a damped harmonic oscillators, modified by the population factor (1):

$$\Phi_i \sim \frac{\Gamma_i f_{0i}^2 f}{(f^2-f_{0i}^2)^2+\Gamma_i^2 f_{0i}^2} F(f,T), \tag{2}$$

where Γ_i and f_{0i} are the damping constant and the mode frequency.

As all of the peaks are much better resolved at low temperatures, we started our fitting procedure at the low-temperature end of the dataset (at 110 K) and then followed the evolution of the peaks with increasing temperature (i.e., in order, opposite to the order of the measurement). We also tried to minimize the number of peaks, necessary to achieve a reasonably good fit. The control dataset (measured without polarization analysis) was used to calibrate the positions and widths of the weak and poorly resolved peaks from the VV and VH datasets. Since a large number of parameters is involved, results of a particular fit may depend on their initial values. To stabilize the results, the best-fit values of parameters obtained at the previous temperature were used as initial values for the next one. In this manner, several sets of fits were obtained and analyzed. It is remarkable that, in all of them, the major parameters followed the same trends of behavior, confirming the importance of the above-mentioned temperatures: $T_d \approx 620 \pm 50$ K, $T^* \approx 350 \pm 25$ K, and $T_{d0} \approx 210 \pm 25$ K. These trends are summarized in Table II. One particular set has been selected to illustrate the most interesting results in detail. Examples of the fits at the temperatures of 1000 and 110 K in VV and VH geometries are shown in Fig. 3. For clarity, we describe the observed phenomena from high to low temperatures, following the same order as in measurements (unless otherwise stated).

IV. MOST INTERESTING RESULTS OF DECOMPOSITION AND THEIR ANALYSIS

A. Central peak

The temperature dependencies of the fitting parameters for the central peak (CP) are presented in Fig. 4. Circles correspond to the VV and triangles to the VH component of the peak. The existence of the CP is a direct consequence of the relaxations, which are very sensitive to the restrictions imposed by the lattice distortions. If relaxations are fast,[58] the CP is nonintense and broad. Their slowing down causes the growth and narrowing of the CP.

We would like to point out a striking similarity in the temperature behavior of the CP in $PbMg_{1/3}Nb_{2/3}O_3$ (Fig. 4) and $KTa_{0.85}Nb_{0.15}O_3$ (Fig. 3 in Ref. 63) crystals. In KTN, we have shown[63] that the temperature behavior of the CP can be explained by a model involving the correlated relaxational motion of off-centered Nb ions in the PNR's and its progressive restriction with decreasing temperature. In the cubic phase, Nb ions are allowed to reorient rapidly amongst eight equivalent $\langle 111\rangle$ directions. In KTN, the sequence of phase transitions from $Pm\bar{3}m$ down to $R3m$ successively restricts the Nb ions to four, then two, and finally to a single site. Since the ion motion within the PNR is correlated, this process can be described as the progressive restriction of the

TABLE II. Major peaks and their response to the temperature restrictions on ion motion. Only changing properties are shown. $T_d \approx 620$ K is also characterized by the total loss of intensity of scattered light.

Peak	Polarization	Region I. Unrestricted dynamical clusters $T \gtrsim (T_d = 620\ \text{K})$	Region II. Restricted dynamical clusters $(T_d = 620\ \text{K}) \gtrsim T \gtrsim (T^* = 350\ \text{K})$	Region III. Formation of static $R3m$ clusters $(T^* = 350\ \text{K}) \gtrsim T$
Central	VV	Intensity decreases broadens	Intensity increases narrows	Intensity has a maximum at 300 K
	VH	Intensity decreases	Intensity increases width has a maximum at 450 K	Intensity has a maximum at 300 K
Peak *A*	VV		Softens, broadens	Hardens and narrows
	VH-I	Broadens	Broadens	Broadens
	VH-II	Softens	Hardens, intensity has minimum at 400 K	Broadens and grows
Peak *C*	VV	Hardens and narrows	Fine structure appears	Splits in two
	VH	Softens	Hardens and narrows	Narrows
Peak *D*	VV		Splits in two	
	VH	Softens	Hardens	Softens and narrows
Peak *F*	VV		VV component appears	VH component appears
Peak *E*	VV		Fine structure appears	Splits in two, VH appears
Peak *B*	VV	Hardening	Hardening	VH appears

PNR orientations. This model is in agreement with the diffuse neutron-scattering studies.[65] The similarity of the CP behavior in these two very different materials suggests that the polar clusters in $PbMg_{1/3}Nb_{2/3}O_3$ pass through similar stages to those in $KTa_{0.85}Nb_{0.15}O_3$ (KTN), although not accompanied by the appearance of long-range order.

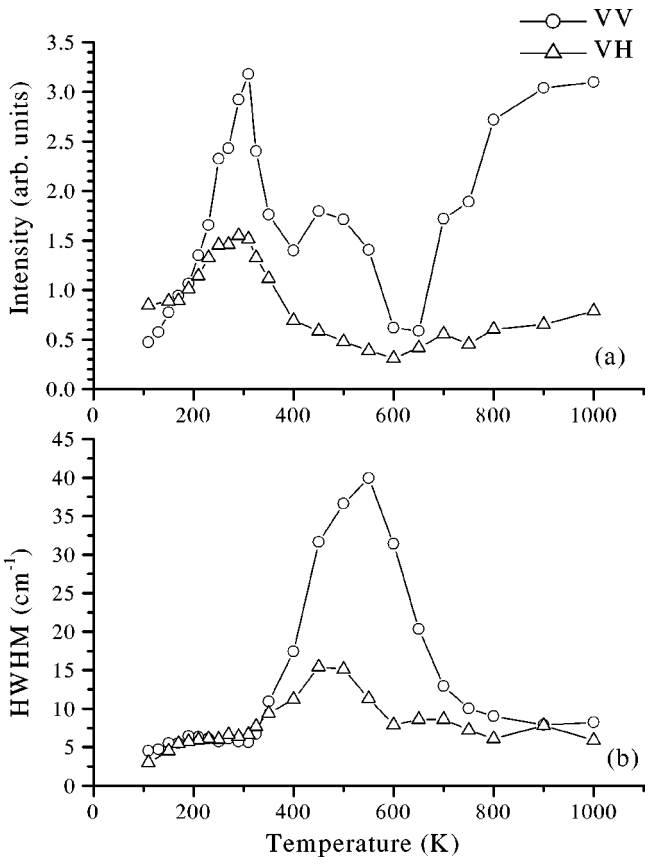

FIG. 4. Temperature dependences of the intensity (a) and half-width (b) of the Lorentzian approximation for the central peak in VV (circles) and VH (triangles) geometries of experiment.

In PMN, starting from high temperature (Fig. 4), the first important feature is the strong and narrow CP in the VV geometry, accompanied by a relatively weak counterpart in the VH geometry. This indicates the presence of a rapid symmetric relaxational motion, involving 180° reorientations of the Nb ions. Lowering the temperature, below ~900 K, the cessation of this motion causes an intensity decrease of the CP. Slow at first, this decrease becomes faster and the CP intensity reaches a minimum near $T_d \approx 620$ K. The prohibition of 180 ° reorientations introduces an anisotropy into the lattice, causing the distinguishability of the Mg and Nb occupied sites and the appearance of a superstructure with a macroscopic (spatially averaged) $Fm\bar{3}m$ symmetry in the 1:1 ordered areas. Below T_d the Nb ions within a PNR can reorient only amongst four neighboring $\langle 111 \rangle$ directions, resulting in a time-averaged local tetragonal distortion. However, the PNR's can still reorient as whole units (or giant dipoles) between several $\langle 100 \rangle$ directions. This process is responsible for the large (of the order of wavelength of light) quasidynamic fluctuations that cause the worsening of the optical quality of the sample.

With further decrease of the temperature, the optical quality of the crystal improves. The renewed increase in the intensities of the VV and VH components of the CP and the increase in both their widths suggest a new quasidynamic range, in which the fluctuations scattering the light correspond to the reorientation of the PNR's. The fact that the respective widths of the two components appear to peak at different temperatures is not unexpected and may reflect the different reorientational modes of the PNR's (e.g., xy, zx, zy). Past their maxima, the decrease in the width of both components down to $T^* \approx 350$ reflects the slowing down of the reorientational dynamics of the PNR's. The analogy with KTN suggests that $T^* \approx 350$ K marks the first of several

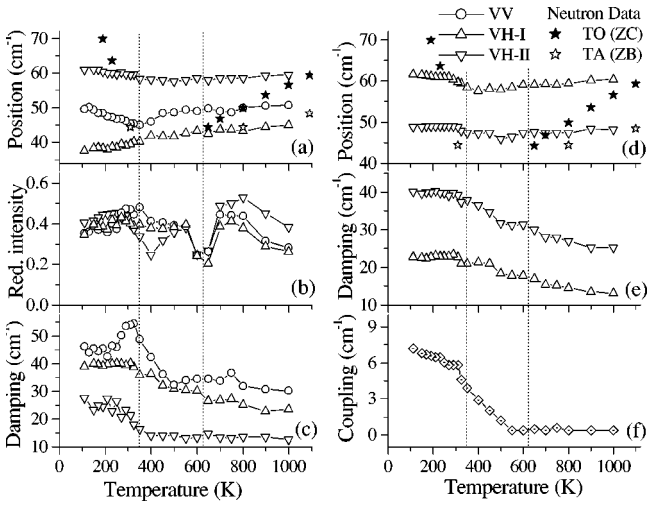

FIG. 5. Temperature dependences of the fitted parameters for the triplet line *A*. Left-hand side shows the model of independent oscillators: position (a), reduced intensity (b), and damping constant (c). Right-hand side shows the model of coupled oscillators (VH): frequency (d), damping constant (e), and coupling coefficient (f). Phonon frequencies (stars), measured by neutron spectroscopy (Refs. 44–47), are shown for comparison.

''underlying'' structural transitions through which the correlated motion of the off-center ions within the PNR's becomes restricted to fewer orientations (two $\langle 111 \rangle$ orientations in KTN). Within this transitional range, the intensities of both VV and VH components go through a maximum, reflecting the structural rearrangements taking place. Further temperature decrease, down to $T_{d0} \approx 210$ K, leads to the off-center ions being restricted to a single position. Below T_{d0}, the central peak is narrow and its intensity remains small in both scattering geometries. The low-temperature phase is most likely composed of $R3m$ PNR's, frozen in random $\langle 111 \rangle$ orientations. When applying an external electric field, this low-temperature phase can be ordered.[24]

We should mention that the result of our analysis of the VV component of the CP exhibits similar tendencies to those in Ref. 50, except at the lower-temperature end. The discrepancy occurs due to differences in experimental techniques. In the central peak region, we did the measurements with a much higher resolution (0.5 cm^{-1}, as compared to 2 cm^{-1} in Ref. 50). Consequently, we are able to provide a more accurate account of the slow relaxations from the quasielastic scattering, which is especially important at low temperatures. To investigate further details, in particular the contribution of the Brillouin scattering, a Fabry-Perot interferometry is necessary (like the one applied to KTN.[54])

B. Line *A*

Figure 5 presents the temperature evolution of the fitting parameters of peak *A*. The left-hand side shows the results of the independent oscillator approach: position [Fig. 5(a)], reduced intensity [Fig. 5(b)], and damping constant [Fig. 5(c)]. This peak has a triplet structure, containing one component in VV (circles) and two components in VH (up and down triangles) geometry. These parameters exhibit changes at above-mentioned temperatures T_d, T^*, and T_{d0}, confirming their importance in the structural evolution of the crystal. However, the origin of this peak (see Table I) requires clarification. From a comparison with the frequencies of the phonon modes determined from neutron scattering, it is clear that this line cannot be due to the zone-center soft TO_1 mode (black stars in Fig. 5). On the other hand, the lower-frequency VH component, and possibly the VV, could be due to disorder-induced zone-boundary scattering by the TA phonon (white stars in Fig. 5). However, the higher-frequency VH component would still not be accounted for.

In an attempt to account for both VH components simultaneously, we have tried to make use of a coupled oscillator model. In the approximation of linear coupling between two harmonic oscillators[66] the intensity is given by

$$I(\omega) = [n(\omega)+1]\left(\frac{CY - BZ}{B^2 + C^2}\right),$$

where

$$B = (\omega_1^2 - \omega^2)(\omega_2^2 - \omega^2) + \omega^2(\gamma_{12}^2 - \gamma_1\gamma_2) - \omega_1\omega_2\Delta_{12}^2,$$

$$C = \omega[\gamma_1(\omega_2^2 - \omega^2) + \gamma_2(\omega_1^2 - \omega^2) - 2(\omega_1\omega_2)^{1/2}\Delta_{12}\gamma_{12}],$$

$$Y = S_1^2(\omega_2^2 - \omega^2) + S_2^2(\omega_1^2 - \omega^2) - 2S_1S_2(\omega_1\omega_2)^{1/2}\Delta_{12},$$

$$Z = \omega(S_1^2\gamma_2 + S_2^2\gamma_1 - 2S_1S_2\gamma_{12}).$$

In these equations ω_1 and ω_2 are the resonant frequencies, γ_1 and γ_2 are the damping constants, S_1 and S_2 are the structure factors for two oscillators, Δ_{12} and γ_{12} are the real and imaginary parts of the coupling constant.

Following Ref. 67, we have chosen to use imaginary coupling and set $\Delta_{12} = 0$. We also set the structure factors S_1 and S_2 to be the same at all temperatures. The rest of the parameters were treated as being temperature dependent. As a result of fitting, we find that the values of the structure factors are $S_1 = 22.3$ cm^{-1} and $S_2 = 20.6$ cm^{-1}. The other parameters are shown on the right-hand side of Fig. 5 as a function of temperature: the best-fit frequencies (d), the damping constants (e), and the coupling coefficient (f).

Examples of the fits (insets in Fig. 3) demonstrate that this model gives a good approximation to the shape of peak *A*. However, a comparison of the best-fit frequencies [Fig. 5(d)] with the neutron-scattering data[44–47] rules out the possibility to explain the higher-frequency VH component by the interaction between ZC TO_1 (black stars) and ZB TA (white stars) modes. The lower-frequency oscillator can still be associated with disorder-induced scattering on the ZB TA mode.

A possible explanation for the presence of two VH components in peak *A* can be their correspondence to coupled phonons with different polarizations.[68] (A similar effect we have seen in monodomain $KTa_{1-x}Li_xO_3$, where one or the other TA polarization was observed, depending on the orientation of a bias electric field.) The coupling is mediated by the disordered lattice distortions, which explains the increase of damping [Fig. 5(e)] and coupling [Fig. 5(f)] coefficients

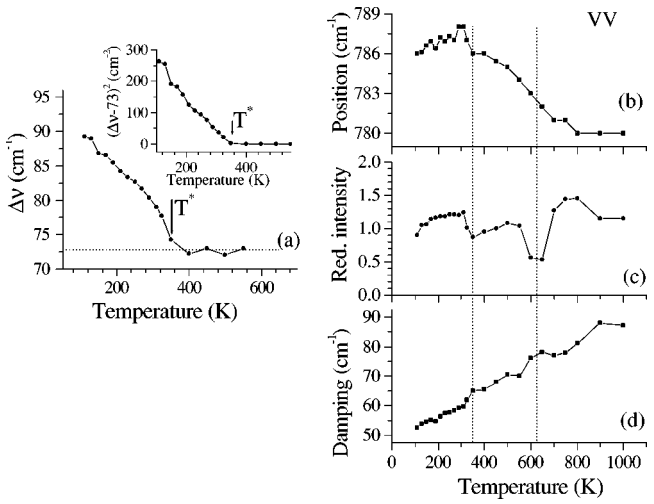

FIG. 6. Left-hand side shows splitting between the components of the line *E* (a). The inset illustrates that it follows the critical dependence law. Right-hand side shows temperature dependences of the fitted parameters for the line *B*: position (b), reduced intensity (c), and damping constant (d).

with lowering temperature. This mediation is also important in explaining the presence of such a strong scattering signal in the VH geometry.

It is also worth pointing out the anomalies in the temperature dependencies of the frequencies of the components of triplet *A* [in an independent oscillator model, Fig. 5(a)] at the intersections with the ZC TO_1 modes (black stars). For example, the VV component exhibits dips at ~700 K and 350 K and the VH-I component has a knee at ~400 K.

C. The most important parameters of other lines

Among the changes occurring in the Raman spectrum with cooling, the splitting and narrowing of the *C*, *D*, and *E* phonon lines deserves special attention, since this splitting is a direct indicator of the lowering of the local symmetry and the narrowing of the Raman lines suggests ordering of the structure. This splitting is especially well seen in the VV geometry [Fig. 2(a)]. At high temperature, these lines are very broad, merging in a single shoulder. Below $T^* \approx 350$ K, a fine structure becomes apparent. These observations support the idea expressed above that the crystal may undergo a succession of ''underlying'' structural transitions. This hypothesis is supported by the trend with temperature of the frequency split between the E_1 and E_2 components, shown in Fig. 6(a). Below T^*, the frequency separation between the two *E* components exhibits a characteristic order parameter behavior, following a $(T^*-T)^{-1/2}$ law [inset to Fig. 6(a)]. Such a trend indeed suggests the existence of a latent phase transformation.[69] Moreover, the ratio of the integral intensities of the two components is found to be equal to 1:2, which could indicate that the frozen low-temperature phase, locally rhombohedral (PNR internal symmetry), is on average (macroscopically) tetragonal. A detailed structural description of the frozen low-temperature phase requires further work and should be the subject of a separate paper.

Finally, we would like to comment on line *B*, located at the high-frequency end of the spectrum. The right-hand side of Fig. 6 shows the fitting parameters for this line: position (b), reduced intensity (c), and damping coefficient (d). This line is very strong in the VV but it is rather weak in the VH geometry (i.e. characterized by A_{1g} symmetry). The temperature evolution of its parameters also reflects the development of the low-temperature phase, confirming the ideas expressed above concerning the formation of the PNR's at $T_d \approx 620$ K, the slowing down of their dynamics through the quasidynamic range and the development of a quasistatic order below $T^* \approx 350$ K. As seen in Table I, this line has been given several contradictory explanations. However, recent first-principles calculations[68] show that this mode is mainly due to the oscillations of the oxygen ion in Mg-O-Nb bonds.

V. CONCLUSION

This paper offers a comprehensive analysis of the Raman-scattering spectra of $PbMg_{1/3}Nb_{2/3}O_3$ in the temperature range between 100 and 1000 K. From our analysis, the structural evolution of the lattice is shown to occur in several characteristic stages. Even at 1000 K, the PMN crystal is characterized by the presence of local dynamic distortions of the lattice from cubic symmetry, which are responsible for the existence of first-order Raman scattering at such a high temperature. At the Burns temperature, $T_d \approx 620$ K, the motion of off-centered ions becomes more correlated, leading to the loss of 180° reorientations and the formation of the polar nanoregions. This causes a distinguishability between sites occupied by Mg and Nb, and the appearance of a macroscopic (spatially averaged) $Fm\bar{3}m$ symmetry in the 1:1 ordered regions. Below T_d, in the quasidynamic range, the correlated motion of off-center ions gives rise to reorientational dynamics of the PNR's, which is seen directly through the evolution of the central peak and, indirectly, through their interaction with phonons. Further cooling leads to progressive growth of restrictions on ionic motion. Below $T^* \approx 350$ K, a quasistatic ordering begins to set in, equivalent to one or several ''underlying'' or latent structural phase transitions, marked by sharper and split phonon peaks. At $T_{d0} \approx 210$ K, this process is complete, resulting in a disordered rhombohedral phase, with a macroscopic (spatially averaged) tetragonal symmetry. The shape of the Raman lines is determined by processes involving phonons with a distribution of wave vectors, interacting with dynamic, quasidynamic, and quasistatic disorder.

ACKNOWLEDGMENTS

Authors are very grateful to D. La-Orauttapong and G. Semenova for helpful discussions. This work was partially supported by the U.S. DOE Grant No. DE.FG02-00ER45842. One of the authors (O.S.) is thankful to V. Dierolf and E. Venger for financial aid.

*On leave for Ph.D. studies from the Institute of Semiconductor Physics, Kyiv 03028, Ukraine.
[1] Z.-G. Ye, Key Eng. Mater. **155-156**, 81 (1998).
[2] V.A. Bokov and I.E. Myl'nikova, Sov. Phys. Solid State, **3**, 613 (1961).
[3] D. Viehland, S.J. Jang, L.E. Cross, and M. Wuttig, Phys. Rev. B **46**, 8003 (1992).
[4] D. Viehland, S. Jang, and L.E. Cross, Philos. Mag. B **64**, 335 (1991).
[5] J. Chen, H.M. Chan, and M.P. Harmer, J. Am. Ceram. Soc. **72**, 593 (1989).
[6] C. Boulesteix, V. Varnier, A. Llebaria, and E. Husson, J. Solid State Chem. **108**, 141 (1994).
[7] S. Miao, J. Zhu, X. Zhang, and Z.-Y. Cheng, Phys. Rev. B **65**, 052101 (2001).
[8] E. Husson, M. Chubb, and A. Morell, Mater. Res. Bull. **23**, 357 (1988).
[9] A.D. Hilton, D.J. Barber, C.A. Randall, and T.R. Shrout, J. Mater. Sci. **25**, 3461 (1990).
[10] M.A. Akbas and P.K. Davies, J. Am. Ceram. Soc. **83**, 119 (2000).
[11] P.K. Davies and M.A. Akbas, J. Phys. Chem. Solids, **61**, 159 (2000).
[12] R. Blinc, A. Gregorovic, B. Zalar, R. Pirc, V.V. Laguta, and M.D. Glinchuk, Phys. Rev. B **63**, 024104 (2001).
[13] I.W. Chen, J. Phys. Chem. Solids **61**, 197 (2000).
[14] T. Egami, W. Dmowski, M. Akbas, and P.K. Davies, in *First-Principles Calculations for Ferroelectrics*, edited by R.E. Cohen, AIP Conf. Proc. **436** (AIP, Woodbury, NY, 1998), p. 1.
[15] E. Husson, L. Abello, and A. Morell, Mater. Res. Bull. **25**, 539 (1990).
[16] G. Burns and F.H. Dacol, Solid State Commun. **48**, 853 (1983); Phys. Rev. B **28**, 2527 (1983).
[17] N. Takesue, Y. Fujii, and H. You, Phys. Rev. B **64**, 184112 (2001).
[18] J. Toulouse, P. DiAntonio, B.E. Vugmeister, X.M. Wang, and L.A. Knauss, Phys. Rev. Lett. **68**, 232 (1992).
[19] P. Bonneau, P. Garnier, G. Calvarin, E. Husson, J.R. Gavarri, A.W. Hewat, and A. Morell, J. Solid State Chem. **91**, 350 (1991).
[20] N. de Mathan, E. Husson, G. Calvarin, J.R. Gavarri, A.W. Hewat, and A. Morell, J. Phys.: Condens. Matter **3**, 8159 (1991).
[21] A. Verbaere, Y. Piffard, Z.-G. Ye, and E. Husson, Mater. Res. Bull. **27**, 1227 (1992).
[22] Y. Uesu, H. Tazawa, K. Fujishiro, and Y. Yamada, J. Korean Phys. Soc. **29**, S703 (1996).
[23] S. Vakhrushev, S. Zhukov, G. Fetisov, and V. Chernyshov, J. Phys.: Condens. Matter **6**, 4021 (1994).
[24] Z.-G. Ye and H. Schmid, Ferroelectrics **145**, 83 (1993).
[25] H. Ohwa, M. Iwata, N. Yasuda, and Y. Ishibashi, Ferroelectrics **229**, 147 (1999); **218**, 53 (1998).
[26] G. Burns and B.A. Scott, Solid State Commun. **13**, 423 (1973).
[27] N.N. Krainik, L.A. Markova, and A.A. Karamjan, Ferroelectrics **143**, 179 (1993).
[28] M. El Marssi, R. Farhi, X. Dai, A. Morell, and D. Viehland, J. Appl. Phys. **80(2)**, 1079 (1996).
[29] M. El Marssi, R. Farhi, and D. Viehland, J. Appl. Phys. **81(1)**, 355 (1997).
[30] M. El Marssi, R. Farhi, M.D. Glinchuk, L. Sedun, and D. Viehland, J. Appl. Phys. **83(10)**, 5371 (1998).
[31] M. El Marssi, R. Farhi, and Yu.I. Yuzyuk, J. Phys.: Condens. Matter **10**, 9161 (1998).
[32] I. Dujovne, T.-Y. Koo, A. Pinczuk, S.-W. Cheong, and B.S. Dennis, Phys. Rev. B **66**, 064110 (2002).
[33] F. Jiang and S. Kojima, Jpn. J. Appl. Phys., Part 1 **38**, 5128 (1999).
[34] S.G. Lushnikov, S.N. Gvasalia, and I.G. Siny, Physica B **263-264**, 286 (1999).
[35] S.G. Lushnikov, S.N. Gvasalia, I.G. Siny, E.A. Goremychkin, and I.L. Sashin, Ferroelectrics **236**, 147 (1999).
[36] I.G. Siny, R.S. Katiar, and S.G. Lushnikov, in *Nanophase and Nanocomposite Materials II*, edited by S. Komarneni, J.C. Parker, and H.J. Wollenberger, Mater. Res. Soc. Symp. Proc. **457** (Materials Research Society, Pittsburg, 1997), p. 39.
[37] I.G. Siny, R.S. Katiar, and A.S. Bhalla, J. Raman Spectrosc. **29**, 385 (1998).
[38] I.G. Siny, S.G. Lushnikov, and R.S. Katiar, Ferroelectrics **231**, 115 (1999).
[39] I.G. Siny and R.S. Katiar, Ferroelectrics **223**, 35 (1999).
[40] I.G. Siny, S.G. Lushnikov, R.S. Katiar, and V.H. Schmidt, Ferroelectrics **226**, 191 (1999).
[41] H. Idink and W. White, J. Appl. Phys. **76**, 1789 (1994).
[42] V. Dimza, P. Paulins, M.S. Zhang, Q. Chen, and Z. Lin, Ferroelectrics **131**, 239 (1992).
[43] B. Mihailova, U. Bismayer, B. Guttler, M. Gospodinov, and L. Konstantinov, J. Phys.: Condens. Matter **14**, 1091 (2002).
[44] P.M. Gehring, S. Wakimoto, Z.-G. Ye, and G. Shirane, Phys. Rev. Lett. **87**, 277601 (2001).
[45] S. Wakimoto, C. Stock, Z.G. Ye, W. Chen, P.M. Gehring, and G. Shirane, cond-mat/0112366 (unpublished).
[46] P.M. Gehring, S.B. Vakhrushev, and G. Shirane, in *Fundamental Physics of Ferroelectrics*, edited by R. Cohen, AIP Conf. Proc. **535** (AIP, Woodbury, NY, 2000), p. 314.
[47] A. Naberezhnov, S. Vakhrushev, B. Dorner, D. Strauch, and H. Moudden, Eur. Phys. J. B **11**, 13 (1999).
[48] T.-Y. Koo, P.M. Gehring, G. Shirane, V. Kiryukhin, G. Lee, and S.-W. Cheong, cond-mat/0110531, (unpublished).
[49] S. Kamba, E. Buixaderas, J. Petzelt, J. Fousek, J. Nosek, and P. Bridenbaugh, J. Appl. Phys. **93**, 933 (2003).
[50] I.G. Siny, S.G. Lushnikov, R.S. Katiyar, and E.A. Rogacheva, Phys. Rev. B **56**, 7962 (1997).
[51] J.P. Sokoloff, L.L. Chase, and D. Rytz, Phys. Rev. B **38**, 597 (1988).
[52] M.D. Fontana, G.E. Kugel, and C. Carabatos-Nedelec, Phys. Rev. B **40**, 786 (1989).
[53] J.P. Sokoloff, L.L. Chase, and D. Rytz, Phys. Rev. B **40**, 788 (1989).
[54] J.P. Sokoloff, L.L. Chase, and L.A. Boatner, Phys. Rev. B **41**, 2398 (1990).
[55] M.D. Fontana, E. Bouziane, and G.E. Kugel, J. Phys.: Condens. Matter **2**, 8681 (1990).
[56] L. Foussadier and M.D. Fontana, Ferroelectrics **153**, 183 (1994).
[57] B.E. Vugmeister, Y. Yacoby, J. Toulouse, and H. Rabitz, Phys. Rev. B **59**, 8602 (1999).
[58] K.H. Michel, J. Naudts, and B. De Raedt, Phys. Rev. B **18**, 648 (1978).
[59] J.M. Rowe, J.J. Rush, and E. Prince, J. Chem. Phys. **66**, 5147 (1977).

[60] J.M. Rowe, J.J. Rush, and S. Susman, Phys. Rev. B **28**, 3506 (1983).
[61] F. Luty, in *Defects in Insulating Crystals*, edited by V.M. Tuchkevich and K.K. Shvarts (Zinatne Publishing House, Riga, 1981), p. 70.
[62] F. Luty, Phys. Rev. B **10**, 3677 (1974).
[63] O. Svitelskiy and J. Toulouse, J. Phys. Chem. Solids **64**, 665 (2003).
[64] Z.-G. Ye, P. Tissot, and H. Schmid, Mater. Res. Bull. **25**, 739 (1990).
[65] G. Yong, J. Toulouse, R. Erwin, S.M. Shapiro, and B. Hennion, Phys. Rev. B **62**, 14 736 (2000).
[66] R. Currat, H. Buhay, C.H. Perry, and A.M. Quittet, Phys. Rev. B **40**, 10741 (1989).
[67] A.S. Barker and J.J. Hopfield, Phys. Rev. **135**, A1732 (1964).
[68] S.A. Prosandeev, E. Cockayne, and B.P. Burton, in *Fundamental Physics of Ferroelectrics*, edited by P. Davies and D. Singh, AIP Conf. Proc. No. **677** (AIP, Woodbury, NY, 2003), p. 146.
[69] I.P. Raevski, S.A. Prosandeev, U. Waghmare, V.V. Eremkin, V.G. Smotrakov, and V.A. Shuvaeva, cond-mat/0208116 (unpublished).